Geometrical impact on the optical polarization of droplet epitaxial quantum dots

Yu-Huai Liao, Chien-Chih Liao, Chih-Hao Ku, Yu-Chen Chang, and Shun-Jen Cheng[*]

Department of Electrophysics, National Chiao Tung University, Hsinchu 30050, Taiwan

Masafumi Jo, Takashi Kuroda, Takaaki Mano, Marco Abbarchi, and Kazuaki Sakoda

National Institute for Materials Science, 1 Namiki, Tsukuba 305-0044, Japan

We report on experimental and theoretical investigations of the optical anisotropy of GaAs/AlGaAs quantum dots grown by droplet epitaxy. With *in situ* annealing in the growth, the shape of quantum dots is systematically controlled from a tall and laterally symmetric shape to a flat and laterally elongated one. Photoluminescence spectroscopy demonstrates an uncommon observation: the more elongated the quantum dots, the lower the degree of linear polarization. Theoretical analysis based on a four-band $\mathbf{k} \cdot \mathbf{p}$ theory reveals a substantial impact of vertical confinement on the valence heavy-hole and light-hole mixing, which leads to the enhancement of polarization anisotropy for taller quantum dots. The influence of Coulomb interactions on polarization anisotropy is studied by using the partial configuration interaction method, and is shown to reduce the polarization anisotropy through the mixing of single-particle configurations with different symmetries.

PACS number(s): 78.67.Hc, 78.55.Cr, 71.35.Cc

I. INTRODUCTION

The polarization state of photons serves as an elementary unit in the quantum communication protocol.[1–3] The photon polarization and the spin state of carriers is in one-to-one correspondence. This fact governs various proposals for manipulating and reading out a single spin confined in a semiconductor quantum dot (QD).[4] Although ideal QDs are expected to show isotropic optical response, any source of symmetry reduction in real QD systems leads to the presence of optical anisotropy, which appears in the anisotropic fine-structure split of neutral excitons,[5–7] as well as linearly polarized (or elliptically polarized) photon emission reflecting the valence-band mixing.[8–12] Such an optical anisotropy is regarded as a core issue for practical applications such as entangled photon generation, exploiting biexciton-exciton recombination cascades,[13–15] and spin initialization schemes with extremely high fidelity.[16,17]

So far, most studies on polarization anisotropies of QDs have been devoted to strained QD systems prepared by the Stranski-Krastanov approach.[8–12,18–20] However, symmetry reduction in these QDs results from a complex interplay between shape asymmetry, nonuniform strain, and composition distributions. Such complexity makes it difficult to find out the true dominant origin of the symmetry breaking in strained QDs.

Theoretically, Sheng and Xu have investigated the effects of shape asymmetry on the linear polarization of InGaAs/GaAs QDs using a tight-binding method.[18] Their study quantitatively predicts the dependencies of the degree of polarization (DOP) on the lateral and vertical aspect ratios of dots, and confirmed composition randomness as a minor effect. The dependencies of DOP on dot shape, however, cannot reflect the pure geometric effect because the strain distribution depends on the shape as well. Very recently, Singh and Bester revealed the spontaneous composition ordering in ternary compounds, such as InGaAs/GaAs self-assembled QDs, as a significant source of DOP besides the shape and strain effects, using empirical pseudopotential computations.[20] Their finding indicates the existence of more uncertainties in the determination of the main physical origins of DOPs in InGaAs/GaAs self-assembled QDs.

The motivation for using GaAs/AlGaAs heterosystems lies in the removal of strain, which enables us to focus on the effects of geometry on optical properties.[21,22] The self-assembly of lattice-matched GaAs/AlGaAs QDs was realized using droplet epitaxy.[23,24] Note that GaAs QDs have been also grown using other techniques.[25,26] Negligible atomic diffusion at the GaAs-AlGaAs interface assures the absence of composition randomness,[27] which has been demonstrated by the cross-sectional tunneling electron microscope analysis.[28] The fine-structure splitting in strain-free GaAs/AlGaAs QDs has been observed previously.[29–31] Significant linear polarizability has been confirmed in the single QD photoluminescence (PL) signals of trions and neutral excitons.[32] They exhibit, however, a broad distribution of the degree of polarization, which thus depends on the microscopic structure of QD that varies from dot to dot. To fully clarify the geometrical effects on optical anisotropy, a more careful experimental setup as well as quantitative theoretical analysis are needed.

This study presents experimental and theoretical investigations of the polarization anisotropy of strain-free GaAs/AlGaAs QDs grown by droplet epitaxy. We focus on a series of QDs with systematically varying lateral elongation and height, achieved by *in situ* annealing in the growth.[33] The anisotropic flow of adsorbed atoms on the (001) surface allows the QD shape to be transformed from a laterally symmetric shape to a laterally elongated one, fabricating unstrained GaAs QDs with controlled shapes over wide ranges of lateral and vertical aspect ratios. Polarized PL spectroscopy reveals that the lateral elongation is not the sole dominant cause of optical anisotropy, as commonly thought.[18] The simplicity of the unstrained GaAs QDs makes an analysis of DOP possible and meaningful, which can be formulated in transparent forms with only a small number of variables and useful for gaining deep physical insight. Theoretical simulations based on the four-band $\mathbf{k} \cdot \mathbf{p}$ theory confirms the essential role of vertical confinement in the observed optical anisotropies.

Using the configuration interaction (CI) method, the effects of Coulombic interactions are studied and shown to diminish the optical anisotropies through the mixing of single-particle configurations with different symmetries.

II. EXPERIMENT

A. Sample preparation and characterization

GaAs QDs studied in this work were grown on the GaAs(001) substrate by droplet epitaxy. The details of this growth are described in our previous work[33] and only briefly summarized herein. Initial deposition of 1.5 monolayers of gallium led to the formation of Ga droplets. Next, an As_4 flux was supplied to crystallize Ga droplets into GaAs QDs. These QDs were then annealed at different temperatures for 10 min under a weak As_4 flux. Finally, they were capped with $Al_{0.35}Ga_{0.65}As$ followed by postgrowth rapid annealing at 800 °C. This sequence is characterized by *in situ* annealing before capping, in which QDs are laterally expanded as their height is reduced. Furthermore, the surface anisotropy of the (001) plane causes the QDs to be elongated in the [1$\bar{1}$0] direction. The magnitude of lateral elongation depends on the annealing temperature. In this work, we study four samples annealed at 400 °C (QD-A), 450 °C (QD-B), 475 °C (QD-C), and 500 °C (QD-D).

The atomic force microscope images of QD-A and QD-B are shown in Figs. 1(a) and 1(b), respectively. They reveal the geometrical variation with annealing temperature. With annealing at 400 °C, the QDs are almost circular in the lateral shape. Annealing at 500 °C, however, considerably lengthens the QDs in the [1$\bar{1}$0] direction.

The cross-sectional profiles parallel to the [1$\bar{1}$0] and [110] axes are also plotted by Figs. 1(c) and 1(d), respectively. A

TABLE I. Geometrical parameters for GaAs QDs annealed at different temperatures. Base length along [1$\bar{1}$0] ([110]) is given by $2\sigma_x$ ($2\sigma_y$), which is determined with the Gaussian fit.

	Temperature (°C)	Base [1$\bar{1}$0] (nm)	Base [110] (nm)	Height (nm)
QD-A	400	68.3 ± 4.8	52.7 ± 6.1	11.1 ± 2.1
QD-B	450	89.1 ± 6.3	57.7 ± 4.5	7.5 ± 1.1
QD-C	475	118 ± 13	55.4 ± 4.7	4.6 ± 1.7
QD-D	500	220 ± 39	64.5 ± 7.9	1.5 ± 0.6

two-dimensional Gaussian function,

$$z = H \exp\{-(x/\sigma_x)^2 - (y/\sigma_y)^2\}, \tag{1}$$

is adopted as a model to describe quantitatively the dot geometries, where $x \parallel$ [1$\bar{1}$0] and $y \parallel$ [110]. As shown in Figs. 1(c) and 1(d), the Gaussian model reproduces the observed profile fairly well. Table I lists the geometrical parameters determined by this fit. As the annealing temperature increases from 400 °C to 500 °C, the base length along [1$\bar{1}$0] increases by a factor of 3, while that along [110] remains almost unchanged. In parallel, the height decreases by a factor of 8.

To characterize the geometrical anisotropy, we define the lateral aspect ratio $\eta_\parallel^{geom}$ and the vertical aspect ratio $\eta_\perp^{geom}$ by

$$\eta_\parallel^{geom} = \sigma_x/\sigma_y, \quad \eta_\perp^{geom} = H/\sigma_y \tag{2}$$

for the QDs of the Gaussian-like shape. Their dependence on the annealing temperature is plotted in Fig. 3(b).

B. Optical measurement

Low-temperature photoluminescence (PL) signals were observed for the ensemble of GaAs QDs after continuous-wave excitation at a wavelength of 532 nm. Photoinjection within this condition was made into the $G_{0.35}Al_{0.65}As$ barrier continuum. Excitation density was kept as low as ~0.1 W cm^{-2}, allowing us to measure PL from the ground-state recombination.[34] Excitation polarization was set to linear to avoid the nuclear effects.[35] In addition, the polarization axis was tilted by ~45° from both of the [110] and [1$\bar{1}$0] crystallographic axis, so as to prevent preferential pumping into the fine-structure split levels.[29] We also confirmed that the PL property was independent of the direction of excitation polarization. The anisotropic transition strengths were therefore assumed to determine the emission polarization.

PL signals emitted normal to the sample surface were fed into a polychromator of 20 cm focal length, followed by a charge-coupled device detector, providing a spectral resolution of 4 meV. A calcite Glan prism and a zeroth-order half-wave plate were adopted as the polarization analyzer. PL spectra were recorded as a function of the rotation angle of the half-wave plate. Then, the degree of linear polarization was calculated by sinusoidal fitting to the intensity modulation with a precision better than 2%. All experiments were performed at 8 K.

Figure 2 shows the PL spectra of GaAs QDs studied in this work. The QD sample annealed at 400 °C (QD-A) shows an inhomogeneously broadened PL peak with a center energy of 1.54 eV. The sample annealed at 450 °C (QD-B) exhibits
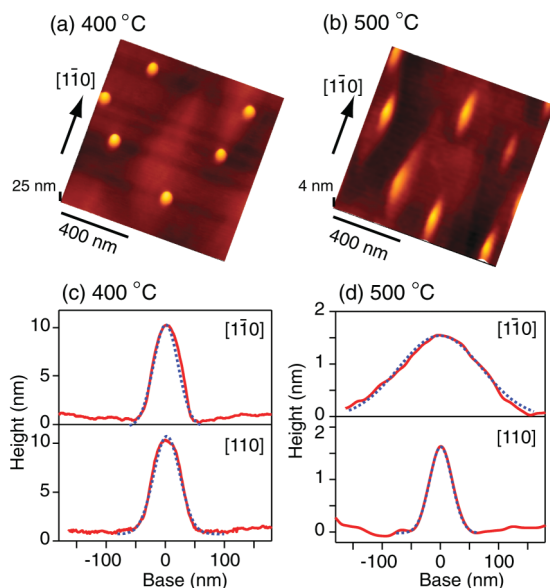

FIG. 1. (Color online) Atomic force microscope images of GaAs QDs annealed at (a) 400 °C and (b) 500 °C before capping. Their vertical cross sections are plotted by solid red lines in (c) and (d), together with Gaussian fits in dotted blue lines.
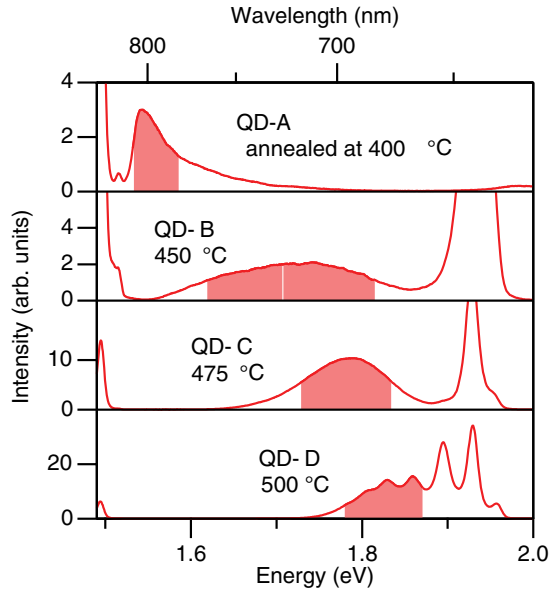
FIG. 2. (Color online) Photoluminescence spectra of GaAs QDs annealed at 400 °C (QD-A), 450 °C (QD-B), 475 °C (QD-C), and 500 °C (QD-D), from top to bottom. A peak at 1.49 eV present in all samples is due to the band-edge luminescence of the GaAs substrate. A peak at 1.93 eV present in QD-B and QD-C is from the wetting layer of 1.5 monolayers on average. The latter peak transforms into multiplets in QD-D, suggesting the formation of the monolayer terraced structure. PL signals are integrated over the shaded area for the polarization analysis shown in Fig. 3.
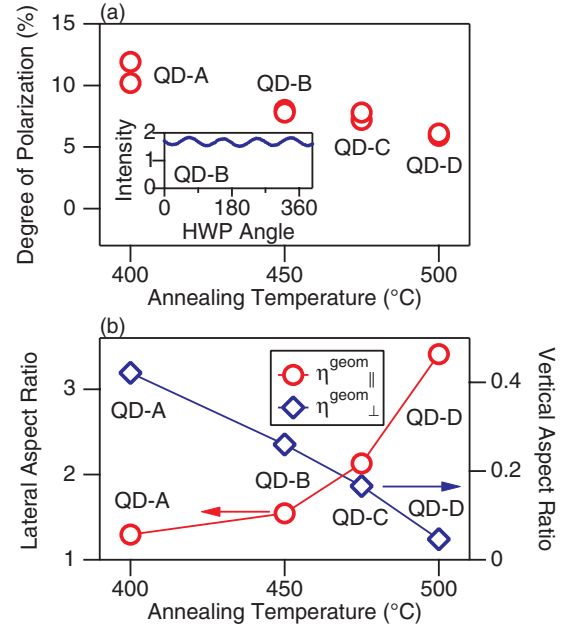

FIG. 3. (Color online) (a) The degree of linear polarization in the PL signals of GaAs QDs annealed at different temperatures. The sign of DOP is defined as positive when $I_{[1\bar{1}0]} > I_{[110]}$. Two sets of data are measured at different positions on the grown sample. The inset shows the dependence of PL intensities on the angle of a half-wave plate (HWP) used in the polarization analyzer. (b) The lateral aspect ratio $\eta_{\parallel}^{\text{geom}}$ and the vertical aspect ratio $\eta_{\perp}^{\text{geom}}$ of GaAs QDs studied in the experiment as a function of annealing temperature.

a broadened peak, with a center energy of 1.72 eV, which is higher than that of QD-A. The blue shift in the PL spectrum reflects the height reduction of QDs by thermal treatment. The sample annealed at 475 °C (QD-C) yields a PL peak at 1.78 eV. The narrower spectrum in QD-C than in QD-B is ascribed to the narrowing of height distribution. Finally, the sample annealed at 500 °C (QD-D) exhibits a further blue shift, and the QD PL band becomes in contact with multiple peaks, which originate from wetting layers with different monolayer thicknesses.

The inset of Fig. 3(a) shows the dependence of PL intensity on the rotating angle of a half-wave plate, where PL signals are integrated over the shading area of each spectrum in Fig. 2. Sinusoidal dependence with a period of 90° demonstrates partial linear polarization in the light field. Throughout this study, we measure the DOP of QDs, which is defined by

$$\text{DOP} = \frac{I_{[1\bar{1}0]} - I_{[110]}}{I_{[1\bar{1}0]} + I_{[110]}}, \qquad (3)$$

where $I_{[1\bar{1}0]}$ ($I_{[110]}$) is the polarized intensity component, whose polarization axis is parallel to the $[1\bar{1}0]$ ($[110]$) in-plane axis. Note that a positive value of DOP appears when $I_{[1\bar{1}0]} > I_{[110]}$. PL in this case is polarized in the direction of lateral elongation of QDs.

Figure 3(a) shows the measured polarization degree for QDs annealed at different temperatures. Figure 3(b) shows the variation of lateral aspect (elongation) ratio $\eta_{\parallel}^{\text{geom}}$ and vertical aspect ratio $\eta_{\perp}^{\text{geom}}$ with annealing temperature. The QDs annealed at 400 °C show a positive DOP of as high as

11 (± 2)%, though lateral elongation is fairly small ($\eta_{\parallel}^{\text{geom}} \leqslant$ 1.2). For QDs annealed at 450 °C, DOP drops to 8 (± 0.05)%, while the lateral elongation is significant ($\eta_{\parallel}^{\text{geom}} = 1.5$). Until the temperature increases to 475 °C ($\eta_{\parallel}^{\text{geom}} \leqslant 2.1$), DOP remains roughly constant. Further increase in the temperature to 500 °C results in a decrease in DOP to 6 (± 0.05)% and elongation of as high as $\eta_{\parallel}^{\text{geom}} = 3.4$. Note that DOP is lower for higher lateral elongation. This trend contradicts the ordinary effect of anisotropy-induced polarization, which has been confirmed in a wide range of quantum confined systems, such as quantum wires. Our observation indicates that lateral anisotropy does not dominate transverse optical polarization in unstrained QDs. Rather, vertical confinement greatly affects DOP, as will be clarified by the theoretical analysis made below.

III. THEORETICAL FRAMEWORK

To account for the experimental findings, the optical polarizations of excitons in three-dimensional (3D) confining QDs are theoretically studied using the partial CI method. The Hamiltonian for an interacting electron-hole pair (an exciton) in a QD is written in second quantization as

$$H_X = \sum_{i_e;\sigma} E_{i_e}^e c_{i_e\sigma}^+ c_{i_e\sigma} + \sum_{i_h;\chi} E_{i_h}^h h_{i_h\chi}^+ h_{i_h\chi}$$
$$- \sum_{i_e,j_h,k_h,l_e} V_{i_e,j_h,k_h,l_e}^{eh} c_{i_e\sigma}^+ h_{j_h\chi}^+ h_{k_h\chi} c_{l_e\sigma}, \qquad (4)$$

where $E_{i_e}^e$ ($E_{i_h}^h$) is the kinetic energy of an electron (hole) on the orbital that is labeled by i_e (i_h), and $h_{i_h}^+$ and h_{i_h} ($c_{i_e}^+$ and c_{i_e}) are the particle creation and annihilation operators, respectively, σ (χ) denotes the spin of the conduction electron (angular momentum of the valence hole), and V_{i_e,j_h,k_h,l_e}^{eh} is the matrix element of the electron-hole e-h Coulomb interactions that are defined by

$$V_{i_e,j_h,k_h,l_e}^{eh} = \iint d\mathbf{r}_e d\mathbf{r}_h \psi_{i_e}^{e*}(\mathbf{r}_e)\psi_{j_h}^{h*}(\mathbf{r}_h)$$
$$\times \frac{e^2}{4\pi\epsilon_0\epsilon_b|\mathbf{r}_e - \mathbf{r}_h|}\psi_{k_h}^h(\mathbf{r}_h)\psi_{l_e}^e(\mathbf{r}_e), \qquad (5)$$

where ψ^e (ψ^h) is the wave function of a single electron (hole) in the dot.

In the presence of Coulomb interactions, an interacting exciton state can be written as a linear combination of coupled electron-hole pair configurations,

$$|\Psi^X\rangle = \sum_{i_h\chi;i_e\sigma} C_{i_h\chi;i_e\sigma} h_{i_h\chi}^+ c_{i_e\sigma}^+ |0\rangle. \qquad (6)$$

The energy spectrum of an exciton in a QD is obtained by solving the Schrödinger equation

$$H_X\Psi_n^X = E_n^X\Psi_n^X \qquad (7)$$

using the partial configuration interaction method, as described in more detail later in Sec. IV B.[36–38]

As the first step in the CI calculation, the single-particle spectra in a QD are calculated using the single-band effective mass model for a conduction electron, and the four-band Luttinger-Kohn $\mathbf{k}\cdot\mathbf{p}$ theory for a valence hole.[39] The separate treatment of a conduction electron and a valence hole is physically acceptable for a wide-energy-gap material like GaAs studied here.

The electron wave function within the single-band model is written as $\psi_{i_e,\sigma}^e(\mathbf{r}) = g_{i_e}^e(\mathbf{r})u_{s_z}^e(\mathbf{r})$, where $g_{i_e}^e(\mathbf{r})$ is the envelope function, $u_{s_z}^e(\mathbf{r})$ is the microscopic Bloch function of the conduction band, and $s_z = +\frac{1}{2}(-\frac{1}{2})$ is the z component of the electron spin $\sigma = \uparrow (\downarrow)$. In the effective mass approximation, the envelope function satisfies the Schrödinger equation

$$\left[\frac{p_e^2}{2m_e^*} + V_{\text{QD}}^e(\mathbf{r}_e)\right] g_{i_e}^e(\mathbf{r}_e) = E_{i_e}^e g_{i_e}^e(\mathbf{r}_e), \qquad (8)$$

where V_{QD}^e is the confining potential and m_e^* is the effective mass of an electron ($m_e^* = 0.067\,m_0$ for GaAs).[40]

For the general application of the theory, we adopt the 3D parabolic model to describe the anisotropic confining potential of an elongated dot,

$$V_{\text{QD}}^e(\mathbf{r}_e) = \sum_{\alpha=x,y,z} \frac{1}{2}m_e^*\omega_{e,\alpha}^2\alpha^2, \qquad (9)$$

where $\omega_{e,\alpha}$ are the characteristic frequencies to specify the degree of confinement along the α direction ($\alpha = x$, y, and z),[41–44] and $l_{e,\alpha} \equiv (\hbar/m_e^*\omega_{e,\alpha})^{1/2}$ denotes the characteristic extent of the wave function. In this model, the single-electron energy spectrum is explicitly given by

$$E_{n_{e,x}n_{e,y}n_{e,z}}^e = \frac{\hbar^2}{m_e}\left[\frac{n_{e,x}+1/2}{(l_{e,x})^2} + \frac{n_{e,y}+1/2}{(l_{e,y})^2} + \frac{n_{e,z}+1/2}{(l_{e,z})^2}\right], \qquad (10)$$

where each electron orbital is labeled by the quantum numbers of a 3D harmonic oscillator, $i_e = (n_{e,x},n_{e,y},n_{e,z})$ with $n_{e,\alpha} = 0, 1, 2, \ldots$. By convention, the Fock-Darwin orbitals of $(n_x,n_y,n_z) = (0,0,0),(1,0,0),(0,1,0),(2,0,0),\ldots$ are denoted by $S, P_x, P_y, D_x, \ldots$, respectively. Note that the wave function of the lowest energy orbital has a Gaussian form,

$$g_{000}^e(\mathbf{r}) = \sqrt{\frac{1}{\pi^{3/2}l_{e,x}l_{e,y}l_{e,z}}} \exp\left[-\frac{1}{2}\left\{\left(\frac{x}{l_{e,x}}\right)^2 \right.\right.$$
$$\left.\left. +\left(\frac{y}{l_{e,y}}\right)^2 + \left(\frac{z}{l_{e,z}}\right)^2\right\}\right]. \qquad (11)$$

Unlike a conduction electron, a single hole that is confined in a QD inherently mixes the heavy-hole (HH) and light-hole (LH) components with the z component of spin, $j_z = \pm\frac{3}{2}$ and $j_z = \pm\frac{1}{2}$, respectively. Within the Kohn-Luttinger four-band $\mathbf{k}\cdot\mathbf{p}$ model, the wave function of a hole is given by $\psi_{i_h}^h(\mathbf{r}_h) = \sum_{j_z=\pm 3/2,\pm 1/2} g_{i_h,j_z}^h(\mathbf{r}_h)u_{j_z}^h(\mathbf{r}_h)$ and satisfies[41,45,46]

$$\begin{pmatrix} P+Q+V_{\text{QD}}^h & -S & R & 0 \\ -S^+ & P-Q+V_{\text{QD}}^h & 0 & R \\ R^+ & 0 & P-Q+V_{\text{QD}}^h & S \\ 0 & R^+ & S^+ & P+Q+V_{\text{QD}}^h \end{pmatrix} \begin{pmatrix} g_{i_h,+\frac{3}{2}}^h \\ g_{i_h,+\frac{1}{2}}^h \\ g_{i_h,-\frac{1}{2}}^h \\ g_{i_h,-\frac{3}{2}}^h \end{pmatrix} = E_{i_h}^h \begin{pmatrix} g_{i_h,+\frac{3}{2}}^h \\ g_{i_h,+\frac{1}{2}}^h \\ g_{i_h,-\frac{1}{2}}^h \\ g_{i_h,-\frac{3}{2}}^h \end{pmatrix}, \qquad (12)$$

where

$$P = \frac{\hbar^2\gamma_1}{2m_0}(\hat{k}_x^2 + \hat{k}_y^2 + \hat{k}_z^2), \quad Q = \frac{\hbar^2\gamma_2}{2m_0}(\hat{k}_x^2 + \hat{k}_y^2 - 2\hat{k}_z^2),$$

$$R = \frac{\hbar^2}{2m_0}[-\sqrt{3}\gamma_3(\hat{k}_x^2 - \hat{k}_y^2) + i2\sqrt{3}\gamma_2\hat{k}_x\hat{k}_y],$$

$$S = \frac{\hbar^2\gamma_3}{2m_0}\sqrt{3}(\hat{k}_x - i\hat{k}_y)\hat{k}_z,$$

and

$$\hat{k}_\alpha = -i\frac{\partial}{\partial\alpha} \quad (\alpha = x,y,z).$$

Here, the Cartesian coordinate system with $\hat{x} \parallel [1\bar{1}0]$, $\hat{y} \parallel [110]$, and $\hat{z} \parallel [001]$ is adopted such that the elongation of QDs is along the x axis. For GaAs, the $\mathbf{k}\cdot\mathbf{p}$ parameters, $\gamma_1 = 6.85$, $\gamma_2 = 2.1$, and $\gamma_3 = 2.9$, are used.[40,47] Although the single-particle states of conduction electron and valence

hole are obtained from the different effective Hamiltonians, Eqs. (8) and (12), they are surely orthogonal to each other because the atomistic basis of their effective Hamiltonians are orthogonal, i.e., $\langle u^e_{s_z} | u^h_{j_z} \rangle = 0$. For simplicity we assume the same confining potentials for HH and LH, which are expressed as

$$
\begin{aligned}
V^h_{\mathrm{QD}}(\mathbf{r}_h) &= \sum_{\alpha=x,y,z} \frac{1}{2} m^*_{\mathrm{HH},\alpha} \omega^2_{\mathrm{HH},\alpha} \alpha^2 \\
&= \sum_{\alpha=x,y,z} \frac{1}{2} m^*_{\mathrm{LH},\alpha} \omega^2_{\mathrm{LH},\alpha} \alpha^2,
\end{aligned}
\tag{13}
$$

where the anisotropic effective masses are written as

$$
m^*_{\mathrm{HH},x(y)} = \frac{1}{\gamma_1 + \gamma_2} m_0, \quad m^*_{\mathrm{HH},z} = \frac{1}{\gamma_1 - 2\gamma_2} m_0, \tag{14}
$$

$$
m^*_{\mathrm{LH},x(y)} = \frac{1}{\gamma_1 - \gamma_2} m_0, \quad m^*_{\mathrm{LH},z} = \frac{1}{\gamma_1 + 2\gamma_2} m_0. \tag{15}
$$

Again, the extent of the HH (LH) wave function is specified as the characteristic length $l_{\mathrm{HH(LH)},\alpha} = (\hbar/m^*_{\mathrm{HH(LH)}}\omega_{\mathrm{HH(LH)},\alpha})^{1/2}$. Throughout this work, we assume that $l_{e,\alpha} = l_{\mathrm{HH},\alpha} \equiv l_\alpha$, yielding constant ratios between $l_{\mathrm{LH},\alpha}$ and $l_{\mathrm{HH},\alpha}$, i.e.,

$$
\begin{aligned}
r_\parallel &\equiv \frac{l_{\mathrm{LH},\,x(y)}}{l_{\mathrm{HH},\,x(y)}} = \left(\frac{m^*_{\mathrm{HH},x(y)}}{m^*_{\mathrm{LH},x(y)}} \right)^{1/4} = \left(\frac{\gamma_1 - \gamma_2}{\gamma_1 + \gamma_2} \right)^{1/4}, \\
r_\perp &\equiv \frac{l_{\mathrm{LH},\,z}}{l_{\mathrm{HH},\,z}} = \left(\frac{m^*_{\mathrm{HH},z}}{m^*_{\mathrm{LH},z}} \right)^{1/4} = \left(\frac{\gamma_1 + 2\gamma_2}{\gamma_1 - 2\gamma_2} \right)^{1/4}.
\end{aligned}
\tag{16}
$$

To parametrize the asymmetry of wave functions confined in an elongated QD, the lateral aspect ratio $\eta_\parallel$ and the vertical aspect ratio $\eta_\perp$ are defined as

$$
\eta_\parallel \equiv l_x/l_y, \quad \eta_\perp \equiv l_z/l_y. \tag{17}
$$

Note that the above aspect ratios of wave functions reflect but are not the same as the geometrical aspect ratios, $\eta^{\mathrm{geom}}_\parallel$ and $\eta^{\mathrm{geom}}_\perp$, which are experimentally defined by Eq. (2).[48]

As will be shown later, the 3D parabolic model allows us, after straightforward algebra, to derive general formalisms in terms of a small number of geometric parameters for describing the polarization properties. The model has been successfully applied to interpret the optical spectra of self-assembled QDs.[49] The analysis carried out in this work is further supported by fully numerical calculations whenever it is possible.

The scope of the model application is discussed as follows. Since this model assumes infinite potential, it is well suitable for describing low-lying excitons but not high-energy ones with the transition energies close to the band gap of the host material. In this study, the sample QD-D is possibly beyond the scope of application because the emission energy was ~ 51.85 eV, close to that of the host material ~ 1.9 eV, as shown in Fig. 2. Another concern of the use of the model is that the geometric parameters $l_{x,y,z}$ are not always proportional to the real dot size with a fixed proportionality constant.[48] Nevertheless, the defined aspect ratios of $\eta_\parallel$ and $\eta_\perp$ should

reflect the real lateral and vertical aspect ratios of dot shape as long as the exciton wave functions are well confined in the QD. For the purpose of grasping the main physics in the measured data of the dot ensembles where individual dots are statistically varied, the model analysis is sufficiently valid for providing qualitatively useful interpretations.

Even within the parabolic model, the energy spectrum of a hole can be calculated only numerically. In this study, the Schrödinger equation of Eq. (12) for a hole in a QD is solved numerically using the 3D finite difference method.[42] From now on, we adopt the quantum numbers of the main HH component, $i_h = (n_{h,x}, n_{h,y}, n_{h,z})'$, to label an HH-LH–mixed orbital and attach a prime superscript to indicate the nature of the HH-LH mixture.

The polarized emission spectrum from an exciton state $|\Psi^X_n\rangle$ of a QD is calculated using Fermi's golden rule,[50]

$$
I_n(\mathbf{e}; \omega) \propto \left| \langle 0 | P^-_{\mathbf{e}} | \Psi^X_n \rangle \right|^2 \delta\left(E^X_n - \hbar\omega \right), \tag{18}
$$

where $P^-_{\mathbf{e}} = \sum_{i_h, i_e} D_{i_h, i_e}(\mathbf{e}) h_{i_h} c_{i_e}$ is the polarization operator, which is given in terms of the dipole matrix elements for various *interband* optical transitions,

$$
D_{i_h, i_e}(\mathbf{e}) \equiv \langle \psi^h_{i_h} | \mathbf{e} \cdot \mathbf{p} | \psi^e_{i_e} \rangle = \sum_{j_z} \langle g^h_{j_h; j_z} | g^e_{i_e; s_z} \rangle \langle u^h_{j_z} | \mathbf{e} \cdot \mathbf{p} | u^e_{s_z} \rangle,
\tag{19}
$$

where $\mathbf{e} = (\cos\phi \sin\theta, \sin\phi \sin\theta, \cos\theta)$ is the unit vector along the direction of polarization of light, and $\mathbf{p} = (-i\partial/\partial x, -i\partial/\partial y, -i\partial/\partial z)$. Here, the spin of the initial conduction electron state is considered to be fixed to $s_z = \frac{1}{2}$ or $s_z = -\frac{1}{2}$. The explicit expressions for the dipole matrix element $\langle u^h_{j_z} | \mathbf{e} \cdot \mathbf{p} | u^e_{s_z} \rangle$ as functions of θ and ϕ can be found in Refs. 41 and 10.

Without HH-LH coupling (as the off-diagonal elements S and R are artificially disabled), a bright exciton with $M_z = s_z + j_z = -1$ ($M_z = +1$) is composed of an electron with $s_z = +\frac{1}{2}$ ($s_z = -\frac{1}{2}$) and a *pure* heavy hole with well-defined spin $j_z = -\frac{3}{2}$ ($j_z = +\frac{3}{2}$), and generates a circularly σ^- (σ^+) polarized photon via spontaneous *e-h* recombination. However, the emission polarization usually deviates from circular and becomes somewhat elliptical or even linear (with DOP $\neq 0$) owing to the HH-LH mixings that arise from the reduced symmetry of the dot structure. Following the definition of DOP in Eq. (3), here the DOP for an exciton in the *n*th state of a QD can be rewritten as

$$
\mathrm{DOP} = \frac{I_n(\hat{x}) - I_n(\hat{y})}{I_n(\hat{x}) + I_n(\hat{y})}, \tag{20}
$$

where $I_n(\hat{e}) \equiv I_n(\hat{e}; \omega = E^X_n/\hbar)$ represents the intensity of the $\hat{e}$-polarized photon emitted from the *n*th exciton state of a QD.

IV. NUMERICAL RESULTS AND ANALYSIS

A. Optical polarization of a noninteracting *e-h* pair

First, we discuss the recombination of a noninteracting *e-h* pair while ignoring Coulomb interactions. In this case, the bright exciton in the ground state is simply written as the product of the single-particle electron and hole wave functions, i.e., $|\Psi^X_{\uparrow\Downarrow}\rangle \approx h^+_{(000)'\Downarrow} c^+_{(000)'\uparrow} |0\rangle$ or $|\Psi^X_{\downarrow\Uparrow}\rangle \approx h^+_{(000)'\Uparrow} c^+_{(000)'\downarrow} |0\rangle$.
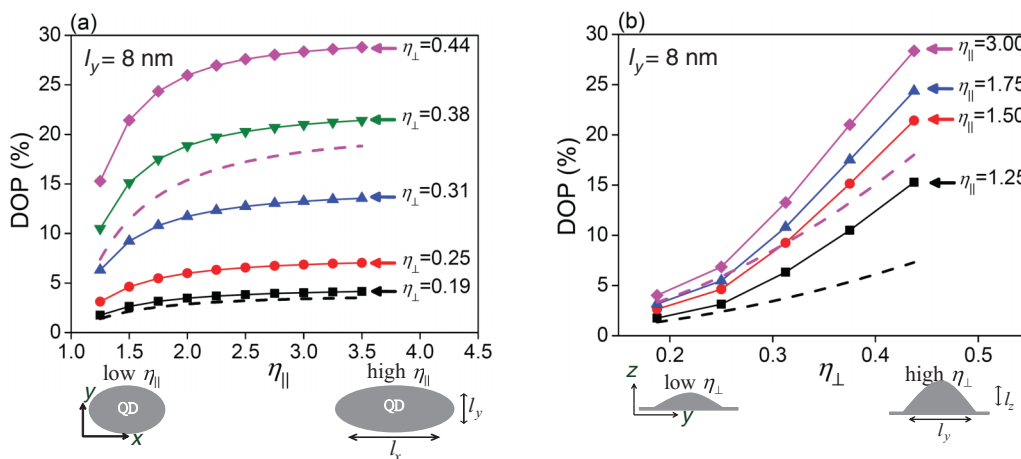
FIG. 4. (Color online) The numerically calculated degrees of polarization (DOPs) as a function of (a) the lateral aspect ratio $\eta_\parallel \equiv l_x/l_y$ and (b) the vertical aspect ratio $\eta_\perp \equiv l_z/l_y$ of elongated quantum dots with fixed $l_y = 8$ nm in the asymmetric parabolic model. In the upper panel (a), the dotted black (dashed magenta) lines are the data obtained from the formula Eq. (A7) for tall QDs with $\eta_\perp = 0.44$ (for flat QDs with $\eta_\perp = 0.19$). In the lower panel (b), the dotted black (dashed magenta) lines are the data obtained from the formula Eq. (A7) for more elongated QDs with $\eta_\perp = 3$ (for less elongated QDs with $\eta_\perp = 1.25$).

Figure 4(a) plots the numerically calculated DOPs versus the lateral aspect ratio $\eta_\parallel = l_x/l_y$ of the lowest exciton states $|\Psi^X_{\uparrow\Downarrow}\rangle$ and $|\Psi^X_{\downarrow\Uparrow}\rangle$ with several magnitudes of $\eta_\perp$. In this plot, we fix the wave-function extension parameter along the y direction to $l_y = 8$ nm, which is determined by the comparison between the analytic wave functions for the parabolic model [Eq. (11)] and the numerically calculated electron wave functions for the real dot shapes. Figure 4(a) shows that DOPs increase but eventually saturate with increasing lateral aspect ratio $\eta_\parallel$.

Figure 4(b) shows the calculated DOPs versus the vertical aspect ratio $\eta_\perp = l_z/l_y$ with a fixed length of $l_y = 8$ nm, and with several magnitudes of lateral elongation $\eta_\parallel$. By contrast to the weak $\eta_\parallel$ dependence shown in Fig. 4(a), a sensitive dependence on $\eta_\perp$ is observed in Fig. 4(b).

As revealed in the Appendix A, the DOP of emitted light is determined by how much the mixture of LH components is in the exciton state. By treating the weak HH-LH mixtures as perturbations for the cases of $l_z \ll l_x, l_y$, the yielded analytical form shows that their DOPs are directly proportional to the magnitude of ρ_{HL}/Δ_{HL} [see Eq. (A6)], where ρ_{HL} is the mean value of the off-diagonal element, and Δ_{HL} the energy separation of HH and LH levels. Equations (A2) and (A3) show that $\rho_{HL} \propto (1 - \eta_\parallel^{-2})$ and $\Delta_{HL} \propto \eta_\perp^{-2} \propto l_z^{-2}$, respectively. The geometric dependence of DOP is therefore written as

$$\text{DOP} \propto \eta_\perp^2 (1 - \eta_\parallel^{-2}). \qquad (21)$$

This shows a quadratic power dependence on the vertical aspect ratio and a relatively weak dependence on the lateral aspect ratio. This fact explains why the less elongated but tall dots in QD-A ensemble have the highest DOP among the annealed dot samples.

The analytic forms of DOP [Eq. (A7)] are also plotted by the dotted line and the broken line in Figs. 4(a) and 4(b). They reproduce numerical results fairly well, except the deviation appearing at large values of $\eta_\perp$ ($\gtrsim 0.3$), which is beyond the validity limit of the perturbation analysis. These results demonstrate how the vertical aspect ratio (height) of

a QD crucially determines DOP, which has been, however, overlooked by most previous studies.

In the experiment we investigated a series of QDs which exhibit a systematic change in the lateral and vertical size with keeping their volume roughly unchanged. Thus, numerical simulations are so made as to follow the experimental shape variation and consider the QDs with a fixed value of characteristic volume $\Omega_l \equiv l_x l_y l_z$ and a fixed length of l_y, but with a variation of l_x and l_z. Figures 5(a) and 5(b) show the calculated DOPs and the PL energies of the lowest-energy, noninteracting *e-h* pairs as a function of the lateral aspect ratio $\eta_\parallel$ for several magnitudes of Ω_l and l_y of the dots, respectively.

A monotonic decrease in DOP with increasing lateral elongation is observed. Based on the simulation, the characteristic length parameter of $l_y = 8$ nm matches best the experimental data. Note that $l_y = 8$ nm was also predicted by the wave-function analysis, as mentioned before. It was also found that the experimental DOPs for small $\eta_\parallel$ agreed with simulations for large Ω_l, and those for large $\eta_\parallel$ agreed with simulations for small Ω_l. Such tendency is consistent with the experimental shape variation, which presented a significant volume reduction for QDs annealed at high temperatures, as was mentioned in Sec. II A.

Analytically, the close form of DOP for fixed Ω_l [Eq. (A8)] can be reformulated as

$$\text{DOP} \propto \frac{\eta_\parallel^2 - 1}{\eta_\parallel^4} \qquad (22)$$

$$\propto \eta_\parallel^{-2} \quad (\eta_\parallel \gg 1). \qquad (23)$$

which also explicitly shows a monotonic decrease in DOP with increasing $\eta_\parallel$. This phenomenon follows from the fact that when the dot volume is kept constant, an increase in lateral elongation leads to a decrease in the dot height, thus leading to a reduction in the HH-LH mixture in the hole state.
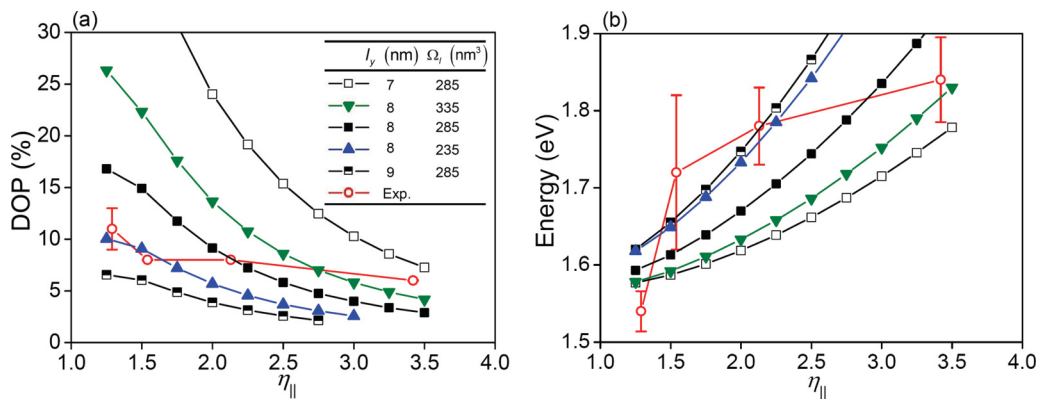
FIG. 5. (Color online) (a) The calculated DOPs and (b) calculated PL energies as functions of the lateral aspect ratio $\eta_\parallel$ for the lowest *noninteracting e-h* combinations of the quantum dots with fixed characteristic length $l_y = 8$ nm and volumes $\Omega_l \equiv l_x l_y l_z = 235$ nm^3, 285 nm^3, and 335 nm^3. Open red circles are experimental data. The error bars present the size/shape distribution of the experimental quantities.

B. Partial configuration interaction calculations: Effects of *e-h* Coulomb interaction

Since the size of GaAs QDs studied in this work is comparable to the effective Bohr radius of bulk excitons (~12 nm for GaAs),[51] interparticle Coulomb interactions in a QD should crucially affect the physical properties. The effect of *e-h* Coulomb interactions on optical anisotropy is investigated below using the CI method.

Within this theoretical framework, first a certain number of relevant single-electron and hole orbitals are selected and used to construct a set of electron-hole pair configurations, which are then used as the basis for expanding the wave functions of the undetermined interacting exciton states. The energy spectrum of single-electron orbitals within the parabolic model are explicitly given by Eq. (10). The evolution of the low-lying energy spectra with respect to the lateral aspect ratio of QD $\eta_\parallel = l_x/l_y$ is shown in Fig. 6(a), in which $l_y = 8$ nm and $\Omega_l = 285$ nm^3 are adopted. The energy spectrum of a single hole in the QD is obtained by solving Eq. (12) numerically using the finite-difference method.[42] Their spectral evolution with respect to $\eta_\parallel$ is shown in Fig. 6(b), which exhibits a complicated feature due to the HH-LH mixing.

Note that a standard implementation of the CI method often utilizes the three- or six-lowest *e* and *h* orbitals to build up the exciton configurations.[19,38] The principle is based on the fact that the degeneracy of the orbital shell follows $g = 1, 2, 3, \ldots$ for a quasi-2D and nearly round-shaped QD. This is however not the case for the highly elongated QDs studied here, where the shell degeneracies are absent in most cases. Thus, the numerical convergence can be obtained simply by increasing the number of selected orbitals one by one until satisfactory convergence is achieved. The exceptions are the dots with special values of the aspect ratios where shell degeneracies are recovered but composed of different orbitals. As a representative case in the measured dot ensemble, the dots with $\eta_\parallel = 2$ (QD-C) have the degeneracies $g = 1, 1, 1, 1, 2, \ldots$, corresponding to the orbitals $(000), (100), (200), (300), \{(010), (400)\}, \ldots$.

In this study, we thus select the six low-lying orbitals listed above and use them to build up the exciton configuration. In principle, there should be $(6 \times 2) \times (6 \times 2) = 144$ configu-

rations that can be constructed from the six spin-degenerate electron and hole orbitals. Among these configurations, we utilize the ones with significant oscillator strengths as the basis set. As a result, a bright exciton state $|\Psi_{\sigma\chi}^X\rangle$ is expanded by the six bright configurations, $h_{000'\chi}^+ c_{000\sigma}^+ |0\rangle$,
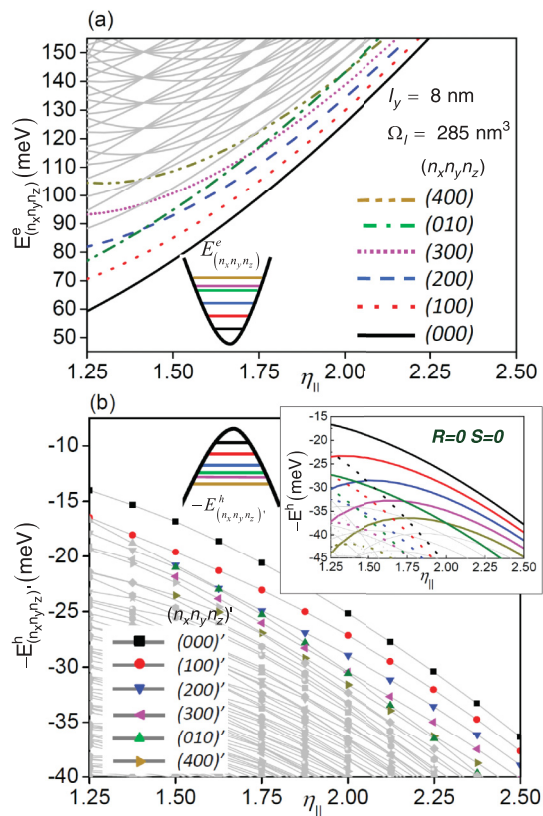

FIG. 6. (Color online) (a) The calculated single-electron energy spectra and (b) the single-hole energy spectra as functions of the lateral aspect ratio $\eta_\parallel$ of the quantum dots with fixed characteristic length $l_y = 8$ nm and volume $\Omega_l = 285$ nm^3. The six lowest levels are labeled by the quantum numbers of the parabolic model. Inset: The pure HH (solid lines) and LH (dotted lines) energy levels of the QD as functions of $\eta_\parallel$, which are yielded from Eq. (12) with the vanishing off-diagonal terms, $S = 0$ and $R = 0$.
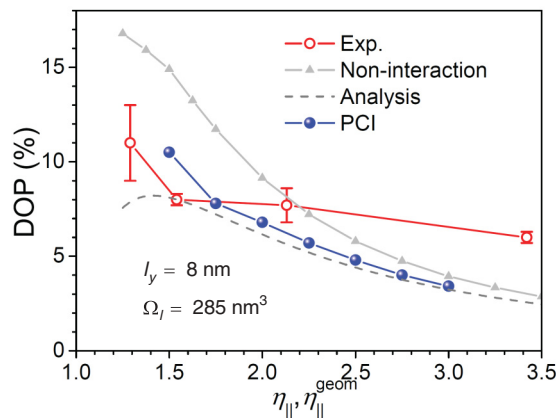
FIG. 7. (Color online) Blue circles: The calculated DOPs as functions of the lateral aspect ratio $\eta_\parallel$ of the exciton ground states of the quantum dots with fixed characteristic length $l_y = 8$ nm and volume $\Omega_l = 285$ nm^3 by using the PCI method. Filled gray triangles: The calculated DOPs for the recombinations of noninteracting *e-h* pairs. Dashed gray line: The DOPs for the recombinations of noninteracting *e-h* pairs yielded by the analytic formalism Eq. (A8). Open red circles: Experimental data.

$h_{100'\chi}^+ c_{100\sigma}^+ |0\rangle$, $h_{010'\chi}^+ c_{010\sigma}^+ |0\rangle$, $h_{200'\chi}^+ c_{200\sigma}^+ |0\rangle$, $h_{300'\chi}^+ c_{300\sigma}^+ |0\rangle$, and $h_{400'\chi}^+ c_{400\sigma}^+ |0\rangle$, which are marked in Figs. 6(a) and 6(b). Thus, the number of the chosen configurations is less than that of all possible ones used for a full CI calculation. Such a simplified way to implement a CI calculation with reduced numerical cost is referred to as the partial configuration interaction (PCI) method in this work. Throughout this work, we consider only the bright neutral excitons with spins $\{\sigma, \chi\} = \{\uparrow, \Downarrow'\}$ or $\{\sigma, \chi\} = \{\downarrow, \Uparrow'\}$. Thus, for brevity we will omit the indices $\{\sigma, \chi\}$ hereafter.

In the reduced basis of exciton configuration, a 6×6 matrix of the Hamiltonian is created, with the Coulomb matrix elements numerically calculated using the integration method used in Ref. 42. The numerical integrations of the Coulomb matrix elements are speeded up significantly by employ-

ing a GPU (graphics processing unit) parallel-computation technique.[52] The energy spectrum and wave functions of the exciton states are obtained by directly diagonalizing the exciton-Hamiltonian matrix using ARPACK eigensolver.[53] Finally, the DOPs of the exciton states of GaAs QDs are calculated using Fermi's golden rule, Eq. (18).

Figure 7 presents the DOPs of the ground-state exciton as a function of the lateral aspect ratio $\eta_\parallel$, with $l_y = 8$ nm and $\Omega_l = 285$ nm^3. To highlight the effect of Coulomb interactions, the DOPs (DOP$_{i_e \to i_h}$) of the noninteracting *e-h* pair configurations $c_{i_e}^+ h_{i_h}^+ |0\rangle$ are also shown for comparison. Both of the simulation results show a qualitative agreement with experimental data but the feature is unusual: the less laterally elongated (but taller) the QDs, the higher the DOPs. The DOPs for the interacting case are qualitatively similar with but generally lower than those for the noninteracting case. The suppression of DOP by the *e-h* Coulomb interactions is even stronger for a less laterally elongated but taller QD.

The analytic formalism of DOP given by the perturbation method [Eq. (A8)] is also plotted in Fig. 7. It is, again, lower than the noninteracting results. This is because the LH components in an exciton state are underestimated by the perturbation method, which is valid only for the weak HH-LH mixing. The results yielded by the two different methods, analytic formalism Eq. (A8) and the PCI calculation, look incidentally similar, but different mechanisms are naturally involved.

The lowering of DOP through the Coulomb interactions is explained as follows. Within the framework of the PCI method, the resulting DOP of an interacting exciton state is averaged by those of each of the configuration components DOP$_{i_e \to i_h}$ weighted by the configuration amplitudes $|C_{i_e i_h}|^2$. Figure 8(a) shows the calculated $|C_{i_e i_h}|^2$ of the six main configurations in the exciton ground states of QDs as a function of $\eta_\parallel$. Apparently, the lowest energy configuration $h_{000'}^+ c_{000}^+ |0\rangle$ dominates the exciton ground states over the whole range of geometrical parameters. Nevertheless, the second-lowest configuration $h_{100'}^+ c_{100}^+ |0\rangle$ also contributes to the exciton ground state in significant manner, and its component increases with $\eta_\parallel$. The increase of the excited configuration component results from the decrease of the energy separation
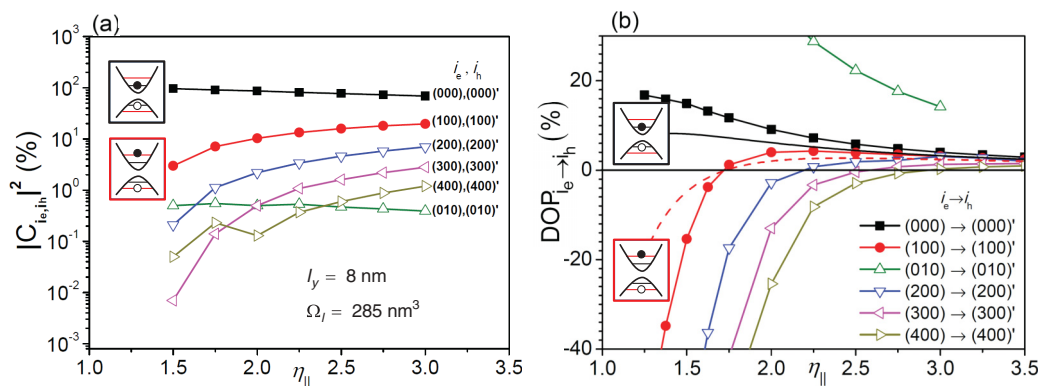

FIG. 8. (Color online) (a) The components $|C_{i_e i_h}|^2$ as functions of the lateral aspect ratio $\eta_\parallel$ of the four main single-particle configurations in the ground state of excitons in the QDs with fixed $l_y = 8$ nm and $\Omega_l = 285$ nm^3 that are calculated using the PCI method. The index $i_e = (n_x n_y n_z)$ [$i_h = (n_x n_y n_z)'$] indicates the filled conduction (valence) orbital by an electron (a valence hole) of the exciton configuration. The schematics in the insets indicate the two dominant configurations in the interacting exciton states. (b) The calculated DOPs for each exciton configuration as functions of $\eta_\parallel$. The black solid line (red broken line) represents the result yielded by the analytic formula [Eqs. (A8) and (A10)].

between (000) and (100) with $\eta_\parallel$, as shown in Figs. 6(a) and 6(b).

Figure 8(b) shows the DOPs of the main e-h pair configuration components. The DOPs of the lowest-energy configuration $h_{000}^+ c_{000}^+ |0\rangle$ decreases with $\eta_\parallel$, as discussed in Sec. IV A. For the x-elongated dots, the second lowest configuration is $h_{100}^+ c_{100}^+ |0\rangle$, which comprises a P_x-like conduction orbital filled by an electron and a P_x-like valence orbital filled by a hole. Their DOPs are generally lower than those of the lowest-energy configuration, and even become negative as $\eta_\parallel$ is sufficiently small. As presented by Eq. (A10) at the end of the Appendix, the analytic form for the DOP of the excited configuration $h_{100}^+ c_{100}^+ |0\rangle$ explicitly shows the same tendency and predicts the sign reversal of DOP at $\eta_\parallel = \sqrt{3}$, which agrees with numerical simulations. Thus, with the mixture of the excited P_x configurations caused by configuration couplings (often referred to as Coulomb correlations), the DOP of an interacting exciton in the ground state is further decreased. In spite of the smaller component amplitude of the P_x configurations for small $\eta_\parallel$, the DOPs are further decreased as $\eta_\parallel \lesssim \sqrt{3}$ because of the rapidly increasing magnitude of the negative DOP of the P_x configurations.

The model analysis conducted above is valid to physically account for our observations. However, a main restriction of the employed four-band $\mathbf{k} \cdot \mathbf{p}$ model for a more precise simulation lies in the poor treatment of the conduction- and valence-band coupling, which is supposedly a weak effect for wide-band-gap semiconductors such as GaAs studied here. Nevertheless, that issue could be essential in the excitonic fine structures of QDs, which are typically at the energy scale of only $\sim$10–100 μeV. The magnitude of fine-structure splitting is obviously much smaller than that of the energy broadening of the measured emission lines from the dot ensembles studied in this work, and is not regarded as within the scope of this study. It is certainly worth extending our currently used model to provide a better quantitative description for optical and fine-structure properties of the unstrained GaAs QDs as a future work, especially as the data of single-dot spectroscopy for the geometry-controlled GaAs QDs become available.

V. SUMMARY

In summary, a systematic, theoretical, and experimental investigation of the optical polarization of shape-controlled GaAs/AlGaAs QDs grown by droplet epitaxy is demonstrated, to a great extent, in this work. The shapes of the quantum dots are varied using the technique of *in situ* thermal treatment during the droplet growth, from a tall and laterally symmetric shape to a flat and elongated one with increasing the annealing temperature. Polarized PL spectroscopy of the QDs reveals an unusual geometry dependence of the optical polarization. Not as commonly known, the less laterally elongated the quantum dots, the higher the degree of linear polarization. Theoretical analysis based on a four-band $\mathbf{k} \cdot \mathbf{p}$ theory shows that the lateral elongation is not the sole dominant cause of optical polarization. Instead, the vertical confinement of a QD crucially determines the valence heavy- and light-hole mixing and the resulting significant optical polarization anisotropy. Therefore, the less elongated but tall QDs show the large

DOPs. The influence of Coulomb interactions on the optical anisotropy is further studied by using the partial configuration interaction method, and is shown to diminish the linear polarization through the mixing of the e-h configurations with different symmetries.

APPENDIX: ANALYTIC EXPRESSION OF DOP UNDER THE PERTURBATION TREATMENT

This Appendix presents the derivation of the analytic forms of the DOP of an HH-LH mixed exciton in a QD under the perturbation treatment. The derived formulation of DOP as a function of the geometric parameters of QD is helpful for gaining physical insight into fully numerical results calculated using the finite-difference method.

We consider the pure HH and LH eigenstates $\{\phi_{n_x n_y n_z}^{HH/LH}\}$ to form a suitable basis set for expanding the HH-like states. Note that the pure HH/LH states are obtained from the four-band Hamiltonian matrix with vanishing off-diagonal terms, $S = 0$ and $R = 0$. If the HH-LH mixture is small, only the leading term $\phi_{000}^{HH/LH}$ in the series of the HH- or LH-envelope function expansion is needed for a qualitative analysis. Thus, in the lowest-order approximation, an effective Hamiltonian is given by a 4×4 matrix in the basis of $\{|\phi_{000}^{HH} u_{+\frac{3}{2}}^h\rangle, |\phi_{000}^{LH} u_{+\frac{1}{2}}^h\rangle, |\phi_{000}^{LH} u_{-\frac{1}{2}}^h\rangle, |\phi_{000}^{HH} u_{-\frac{3}{2}}^h\rangle\}$ for a HH-LH-mixed hole in a QD:[10–12]

$$
\begin{pmatrix}
E_{HH} & 0 & \rho_{HL} & 0 \\
0 & E_{HH} + \Delta_{HL} & 0 & \rho_{HL} \\
\rho_{HL}^\dagger & 0 & E_{HH} + \Delta_{HL} & 0 \\
0 & \rho_{HL}^\dagger & 0 & E_{HH}
\end{pmatrix}, \quad \text{(A1)}
$$

where $E_{HH} = \langle \phi_{000}^{HH} | P + Q + V_{QD}^h | \phi_{000}^{HH} \rangle$ is the kinetic energy of pure HH, $\Delta_{HL} \approx -\langle \phi_{000}^{HH} | Q | \phi_{000}^{HH} \rangle - \langle \phi_{000}^{LH} | Q | \phi_{000}^{LH} \rangle$ is the energy separation between the decoupled HH and LH levels, and $\rho_{HL} \equiv \langle \phi_{000}^{HH} | R | \phi_{000}^{LH} \rangle$ is the matrix element of the HH-LH coupling. Another off-diagonal term $\langle \phi_{000}^{HH} | S | \phi_{000}^{LH} \rangle \propto \langle \phi_{000}^{HH} | k_x k_z - i k_y k_z | \phi_{000}^{LH} \rangle$ vanishes since the basis function ϕ_{000} has the mirror symmetries in the x, y, and z directions. The model Hamiltonian of Eq. (A1) has been employed in the previous studies of Refs. 10 and 11.

Furthermore, the matrix elements in Eq. (A1) can be explicitly expressed as functions of the geometric parameters l_α and $\eta_\parallel$ of QD in the 3D parabolic model,

$$
\rho_{HL} \approx \frac{4 r_\parallel}{(1 + r_\parallel^2)^2} \frac{\sqrt{3} \hbar^2 \gamma_3}{4 m_0} \times \frac{1}{l_y^2} \left(1 - \frac{1}{\eta_\parallel^2} \right) \quad \text{(A2)}
$$

and

$$\Delta_{\mathrm{HL}} = \frac{\hbar^2 \gamma_2}{m_0} \times \left(\frac{1+r_\perp^2}{r_\perp^2 l_z^2} - \frac{1+r_\parallel^2}{2r_\parallel^2 l_x^2} - \frac{1+r_\parallel^2}{2r_\parallel^2 l_y^2} \right)$$

$$\approx \left(\frac{1+r_\perp^2}{r_\perp^2} \right) \frac{\hbar^2 \gamma_2}{m_0} \times \frac{1}{l_z^2} \quad (l_x, l_y \gg l_z), \quad \text{(A3)}$$

where the parameters $r_{\parallel/\perp}$ defined in Eq. (16) are used to characterize the anisotropy of the HH and LH masses.

Treating the HH-LH coupling terms in Eq. (A1) as perturbations ($|\rho_{\mathrm{HL}}/\Delta_{\mathrm{HL}}| \ll 1$) yields the ground state of a single hole,

$$\psi_{(000)'}^h(\mathbf{r}_h) \propto \phi_{000}^{\mathrm{HH}}(\mathbf{r}_h) u_{\pm\frac{3}{2}}^h(\mathbf{r}_h) - \frac{\rho_{\mathrm{HL}}}{\Delta_{\mathrm{HL}}} \phi_{000}^{\mathrm{LH}}(\mathbf{r}_h) u_{\mp\frac{1}{2}}^h(\mathbf{r}_h) + \cdots .$$

$$\text{(A4)}$$

Equation (A4) reveals that the HH-LH mixtures of the hole state directly depend on the quantity ($\rho_{\mathrm{HL}}/\Delta_{\mathrm{HL}}$). Accordingly, more HH-LH mixtures in the hole state could result from either a higher value of ρ_{HL} or a lower value of Δ_{HL}, each of which, however, follow different dependencies on the geometry of QD, as given by Eqs. (A2) and (A3), respectively. $\rho_{\mathrm{HL}} \propto (1 - \eta_\parallel^{-2})$ is governed by the lateral elongation of QDs, and it becomes higher for higher elongation. $\Delta_{\mathrm{HL}} \propto l_z^{-2}$ is, on the other hand, governed by the vertical height of QDs, and it becomes higher for taller QDs. Compared with the weak dependence of ρ_{HL} on $\eta_\parallel$, the Δ_{HL} follows a stronger quadratic dependence of the power on the height of the dot. Therefore, the height or the vertical aspect ratio of a planar QD crucially determines the HH-LH mixing and, as shown below, the optical anisotropies of an exciton in a QD as well.

Taking into account the HH-LH mixture given by Eq. (A4) in the hole states, the degree of transverse polarization [with the substitution of $\mathbf{e} = (\cos\phi, \sin\phi, 0)$ into Eq. (18)] for the non-interacting e-h pairs, $\approx h_{(000)'\downarrow}^+ c_{(000)\uparrow}^+ |0\rangle$ and $h_{(000)'\uparrow}^+ c_{(000)\downarrow}^+ |0\rangle$, is derived as[10,11]

$$\mathrm{DOP}_{(000) \to (000)'} \approx \frac{2|\rho_{\mathrm{HL}}|/\sqrt{3}\Delta_{\mathrm{HL}}}{1 + (|\rho_{\mathrm{HL}}|/\sqrt{3}\Delta_{\mathrm{HL}})^2}. \quad \text{(A5)}$$

For a weak HH-LH mixture ($|\rho_{\mathrm{HL}}|/\Delta_{\mathrm{HL}} \ll 1$), the formula for the DOP of a QD can be further simplified and written in terms of the geometric parameters of QD as

$$\mathrm{DOP}_{(000) \to (000)'} \approx \frac{2|\rho_{\mathrm{HL}}|}{\sqrt{3}\Delta_{\mathrm{HL}}} \quad \text{(A6)}$$

$$= F \times \frac{\gamma_3 \eta_\perp^2}{2\gamma_2} \left(\frac{\eta_\parallel^2 - 1}{\eta_\parallel^2} \right) \quad \text{(A7)}$$

$$= F \times \frac{\gamma_3 \Omega_l^2}{2\gamma_2 l_y^6} \left(\frac{\eta_\parallel^2 - 1}{\eta_\parallel^4} \right), \quad \text{(A8)}$$

where the factor $F \equiv 8r_\parallel r_\perp^2 / (1 + r_\parallel^2)^2 (1 + r_\perp^2) \neq 1$ as the HH and LH wave functions is not symmetric ($l_{\mathrm{HH},x(y)} \neq l_{\mathrm{LH},x(y)}$). The above expressions clearly elucidate the effects of the geometry and size of a dot on optical polarization.

The same derivation procedure can be used to derive the DOPs for higher-energy transitions between a single-electron level $i_e = (n_x n_y n_z)$ and single-hole level $i_h = (n_x n_y n_z)'$,

$$\mathrm{DOP}_{(n_x, n_y, n_z) \to (n_x, n_y, n_z)'}$$

$$\propto \frac{\gamma_3 \Omega_l^2}{(2n_z + 1)\gamma_2 l_y^6} \left\{ \frac{(2n_y + 1)\eta_\parallel^2 - (2n_x + 1)}{\eta_\parallel^4} \right\}. \quad \text{(A9)}$$

The above expressions explicitly show that the DOP is always positive if $\eta_\parallel > 1$ and $n_x < n_y$. For the optical transitions that involve the orbitals with $n_x > n_y$, the DOP is positive only if $\eta_\parallel$ is large enough, and becomes negative for high lateral elongation along x. For instance, the DOP that involves the first excited electron and hole orbital ($n_x = 1, n_y = 0, n_z = 0$) of a QD is explicitly given by

$$\mathrm{DOP}_{(100) \to (100)'} = \frac{16r_\parallel^2 r_\perp^2}{(1 + r_\parallel^2)^3 (1 + r_\perp^2)} \times \frac{\gamma_3 \eta_\perp^2}{2\gamma_2} \left(\frac{\eta_\parallel^2 - 3}{\eta_\parallel^2} \right). \quad \text{(A10)}$$

The geometric dependence in Eq. (A10) is plotted in Fig. 8(a) together with the numerical result. It shows that DOP changes from positive to negative with decreasing $\eta_\parallel$ at the critical lateral aspect ratio estimated to be $\eta_\parallel = \sqrt{3}$, consistent with the numerical result in Fig. 8(a).

---

*sjcheng@mail.nctu.edu.tw

[1] P. Kok, W. J. Munro, K. Nemoto, T. C. Ralph, J. P. Dowling, and G. J. Milburn, Rev. Mod. Phys. **79**, 135 (2007).

[2] N. Gisin, G. Ribordy, W. Tittel, and H. Zbinden, Rev. Mod. Phys. **74**, 145 (2002).

[3] P. G. Kwiat, K. Mattle, H. Weinfurter, A. Zeilinger, A. V. Sergienko, and Y. Shih, Phys. Rev. Lett. **75**, 4337 (1995).

[4] *Semiconductor Quantum Bits*, edited by F. Henneberger and O. Benson (Pan Stanford, Singapore, 2009).

[5] D. Gammon, E. S. Snow, B. V. Shanabrook, D. S. Katzer, and D. Park, Phys. Rev. Lett. **76**, 3005 (1996).

[6] M. Bayer, G. Ortner, O. Stern, A. Kuther, A. A. Gorbunov, A. Forchel, P. Hawrylak, S. Fafard, K. Hinzer, T. L. Reinecke, S. N. Walck, J. P. Reithmaier, F. Klopf, and F. Schäfer, Phys. Rev. B **65**, 195315 (2002).

[7] R. Seguin, A. Schliwa, S. Rodt, K. Pötschke, U. W. Pohl, and D. Bimberg, Phys. Rev. Lett. **95**, 257402 (2005).

[8] A. V. Koudinov, I. A. Akimov, Y. G. Kusrayev, and F. Henneberger, Phys. Rev. B **70**, 241305 (2004).

[9] D. N. Krizhanovskii, A. Ebbens, A. I. Tartakovskii, F. Pulizzi, T. Wright, M. S. Skolnick, and M. Hopkinson, Phys. Rev. B **72**, 161312 (2005).

[10] Y. Léger, L. Besombes, L. Maingault, and H. Mariette, Phys. Rev. B **76**, 045331 (2007).

[11] C. H. Lin, W. T. You, H. Y. Chou, S. J. Cheng, S. D. Lin, and W. H. Chang, Phys. Rev. B **83**, 075317 (2011).

[12] S. Ohno, S. Adachi, R. Kaji, S. Muto1, and H. Sasakura, Appl. Phys. Lett. **98**, 161912 (2011).

[13] O. Benson, C. Santori, M. Pelton, and Y. Yamamoto, Phys. Rev. Lett. **84**, 2513 (2000).

[14] R. M. Stevenson, R. J. Young, P. Atkinson, K. Cooper, D. A. Ritchie, and A. J. Shields, Nature (London) **439**, 179 (2006).

[15] N. Akopian, N. H. Lindner, E. Poem, Y. Berlatzky, J. Avron, D. Gershoni, B. D. Gerardot, and P. M. Petroff, Phys. Rev. Lett. **96**, 130501 (2006).

[16] M. Atature, J. Dreiser, A. Badolato, A. Hogele, K. Karrai, and A. Imamoglu, Science **312**, 551 (2006).

[17] B. D. Gerardot, D. Brunner, P. A. Dalgarno, P. Ohberg, S. Seidl, M. Kroner, K. Karrai, N. G. Stoltz, P. M. Petroff, and R. J. Warburton, Nature (London) **451**, 441 (2008).

[18] W. Sheng and S. J. Xu, Phys. Rev. B **77**, 113305 (2008).

[19] V. Mlinar and A. Zunger, Phys. Rev. B **79**, 115416 (2009).

[20] R. Singh and G. Bester, Phys. Rev. B **84**, 241402 (2011).

[21] J. W. Luo and A. Zunger, Phys. Rev. B **84**, 235317 (2011).

[22] V. Mlinar, A. Schliwa, D. Bimberg, and F. M. Peeters, Phys. Rev. B **75**, 205308 (2007).

[23] N. Koguchi, S. Takahashi, and T. Chikyow, J. Cryst. Growth **111**, 688 (1991).

[24] K. Watanabe, N. Koguchi, and Y. Gotoh, Jpn. J. Appl. Phys. **39**, L79 (2000).

[25] M. H. Baier, S. Watanabe, E. Pelucchi, and E. Kapon, Appl. Phys. Lett. **84**, 1943 (2004).

[26] A. Rastelli, S. Stufler, A. Schliwa, R. Songmuang, C. Manzano, G. Costantini, K. Kern, A. Zrenner, D. Bimberg, and O. G. Schmidt, Phys. Rev. Lett. **92**, 166104 (2004).

[27] T. E. Schlesinger and T. Kuech, Appl. Phys. Lett. **49**, 519 (1986).

[28] J. G. Keizer, J. Bocquel, P. M. Koenraad, T. Mano, T. Noda, and K. Sakoda, Appl. Phys. Lett. **96**, 062101 (2010).

[29] M. Abbarchi, C. A. Mastrandrea, T. Kuroda, T. Mano, K. Sakoda, N. Koguchi, S. Sanguinetti, A. Vinattieri, and M. Gurioli, Phys. Rev. B **78**, 125321 (2008).

[30] T. Mano, M. Abbarchi, T. Kuroda, B. McSkimming, A. Ohtake, K. Mtsuishi, and K. Sakoda, Appl. Phys. Express **3**, 065203 (2010).

[31] J. D. Plumhof, V. Krapek, L. Wang, A. Schliwa, D. Bimberg, A. Rastelli, and O. G. Schmidt, Phys. Rev. B **81**, 121309 (2010).

[32] T. Belhadj, T. Amand, A. Kunold, C. M. Simon, T. Kuroda, M. Abbarchi, T. Mano, K. Sakoda, S. Kunz, X. Marie, and B. Urbaszek, Appl. Phys. Lett. **97**, 051111 (2010).

[33] M. Jo, T. Mano, and K. Sakoda, Appl. Phys. Express **3**, 045502 (2010).

[34] K. Kuroda, T. Kuroda, K. Watanabe, T. Mano, K. Sakoda, G. Kido, and N. Koguchi, Appl. Phys. Lett. **90**, 051909 (2007).

[35] T. Belhadj, T. Kuroda, C.-M. Simon, T. Amand, T. Mano, K. Sakoda, N. Koguchi, X. Marie, and B. Urbaszek, Phys. Rev. B **78**, 205325 (2008).

[36] A. Schliwa, M. Winkelnkemper, and D. Bimberg, Phys. Rev. B **79**, 075443 (2009).

[37] S. J. Cheng, Phys. Rev. B **76**, 075329 (2007).

[38] P. Hawrylak, Phys. Rev. B **60**, 5597 (1999).

[39] J. M. Luttinger, Phys. Rev. **102**, 1030 (1956).

[40] S. L. Chuang, *Physics of Photonic Devices* (Wiley, Hoboken, 2009).

[41] J. Kumar, S. Kapoor, S. K. Gupta, and P. K. Sen, Phys. Rev. B **74**, 115326 (2006).

[42] H. Y. Ramirez, C. H. Lin, C. C. Chao, Y. Hsu, W. T. You, S. Y. Huang, Y. T. Chen, H. C. Tseng, W. H. Chang, S. D. Lin, and S. J. Cheng, Phys. Rev. B **81**, 245324 (2010).

[43] H. Y. Ramirez and S. J. Cheng, Phys. Rev. Lett. **104**, 206402 (2010).

[44] Y. T. Chen, S. J. Cheng, and C. S. Tang, Phys. Rev. B **81**, 245311 (2010).

[45] F. B. Pedersen and Y. C. Chang, Phys. Rev. B **53**, 1507 (1996).

[46] J. I. Climente, M. Korkusinski, G. Goldoni, and P. Hawrylak, Phys. Rev. B **78**, 115323 (2008).

[47] J. Los, A. Fasolino, and A. Catellani, Phys. Rev. B **53**, 4630 (1996).

[48] According to the 3D finite-difference simulation for the electron wave functions of the QDs described by Eq. (1), the relations between the aspect ratios of particle wave function and those of dot shapes are approximately given by $\eta_\parallel \approx \eta_\parallel^{geom}$ and $\eta_\perp \approx c\eta_\perp^{geom}$, with $c = 2 \sim 4$.

[49] S. Raymond, S. Studenikin, A. Sachrajda, Z. Wasilewski, S. J. Cheng, W. Sheng, P. Hawrylak, A. Babinski, M. Potemski, G. Ortner, and M. Bayer, Phys. Rev. Lett. **92**, 187402 (2004).

[50] W. Sheng, S. J. Cheng, and P. Hawrylak, Phys. Rev. B **71**, 035316 (2005).

[51] H. Fu, L. W. Wang, and A. Zunger, Phys. Rev. B **59**, 5568 (1999).

[52] NVIDIA CUDA Compute Unified Device Architecture Programming Guide, http://www.nvidia.com/cuda.

[53] R. B. Lehoucq, D. C. Sorensen, and C. Yang, ARPACK Users' Guide (SIAM, Philadelphia, 1998).